frontiers | Frontiers in Earth Science

TYPE Original Research
PUBLISHED 08 June 2023
DOI 10.3389/feart.2023.1102785

OPEN ACCESS

EDITED BY
Nadia Solovieva,
University College London,
United Kingdom

REVIEWED BY
Jef Vandenberghe,
VU Amsterdam, The Netherlands
Taejin Choi,
Korea National University of Education,
Republic of Korea

*CORRESPONDENCE
Seungwon Shin,
ssw7304@kangwon.ac.kr

RECEIVED 19 November 2022
ACCEPTED 11 May 2023
PUBLISHED 08 June 2023

CITATION
Lee J-Y, Shin S, Yoon HH, Kim JC, Choi Y, Nahm W-H and Kim H (2023), The Sedimentary records of the Hapcheon impact crater basin in Korea over the past 1.3 Ma.
Front. Earth Sci. 11:1102785.
doi: 10.3389/feart.2023.1102785

The Sedimentary records of the Hapcheon impact crater basin in Korea over the past 1.3 Ma

Jin-Young Lee[1], Seungwon Shin[2]*, Hyun Ho Yoon[1], Jin Cheul Kim[1], Yire Choi[3], Wook-Hyun Nahm[1] and Heejung Kim[2]

[1]Climate Change Response Research Division, Korea Institute of Geosciences and Mineral Resources, Daejeon, Republic of Korea, [2]Division of Geology and Geophysics, Kangwon National University, Gangwon, Republic of Korea, [3]Geologic Hazards Research Division, Korea Institute of Geosciences and Mineral Resources and Mineral Resources, Daejeon, Republic of Korea

The Hapcheon impact crater is the only meteorite impact crater identified on the Korean peninsula. However, the morphology of the impact crater and the nature of the meteorite collision are unknown. In this study, we analyzed the sedimentary facies using grain size data; computed tomography images, ^{14}C, ^{10}Be, and optically stimulated luminescence dating on a >66-m-long sediment core (20HCL04) recovered from the Hapcheon Basin. Four sedimentary units and 10 types of facies were documented in the Hapcheon Basin sediment core. The sedimentary units comprise 1) a lower part (unit 1) that is dominated by moderately to well-sorted coarse gravel, which contains some impact-related sediments; 2) a middle part (units 2 and 3) dominated by well-laminated mud; and 3) an upper part (Unit 4) that is dominated by poorly sorted coarse gravel supplied from the surrounding mountain slopes by alluvial and fluvial processes. After the meteorite impact, the Hapcheon impact crater was filled with deposits from the crater wall after *ca*. 1.3 Ma and the Hapcheon Basin became a deep lake environment. After *ca*. 0.5 Ma, sediments were supplied from the surrounding mountains until the lake was filled. Finally, sediments were deposited in an alluvial fan setting. In addition, the Hapcheon Basin sedimentary cores contain a tephra layer and deformed soft sediments that can be used to investigate volcanic and seismic events on the Korean Peninsula over the past 1.3 Ma.

KEYWORDS

Hapcheon Basin, impact crater, lake environment, middle quaternary, Korean peninsula

1 Introduction

Meteorite impact events have occurred regularly on Earth, and numerous studies of meteorite impact craters have been conducted worldwide. Studies of meteorite impact craters have been focused mainly on Europe and the Americas, with very few meteorite impact craters identified in Asia. The Hapcheon impact crater basin is located in the Jeokjung–Chogye area of the city of Hapcheon, which is in the southern–central part of the Korean Peninsula. The impact crater was described by Lim et al. (2021). Choi S. et al. (2022) suggested that the center of the peak ring is located ~350 m to the west of the center of the exterior ring, based on gravity data, and that the bedrock under the uplift ring was uplifted ~200 m following the meteorite impact. Choi S. H. et al. (2022) investigated the impact origin of the structure, inferred the potential projectile, and suggested that the impactites contained ~0.05 wt% of a chondritic component.

Some global examples of meteorite impact craters are lakes undergoing active sedimentation (Fredriksson et al., 1973; Guyard et al., 2011; Melles et al., 2011; Shanahan et al., 2012; Reimold and Koeberl, 2014; Losiak et al., 2016; Lim et al., 2021). Meteorite impact craters have been reported worldwide, including in the oceans (Jones et al., 1981; Reimold et al., 1998; Gurov et al., 2007; Liu et al., 2013; Reimold and Koeberl, 2014; Retzler et al., 2015; Ebinghaus et al., 2017; McLean et al., 2018). The Hapcheon meteorite impact crater currently has a small basin shape, containing >100 m of sediment, and a >72 m thick sediment layer has been reported in the lake (Lim et al., 2021).

Lakes with closed sedimentary systems, such as those formed by volcanic craters and large tectonic structures, record past climate and sedimentary information. For example, a crater formed by volcanic activity is generally infilled with volcanogenic sediments and has a bowl-shaped geomorphology. In terms of the sedimentary accommodation space created by a meteorite impact, an impact crater is similar to a volcanic crater, which has been well-documented in numerous previous studies (Osinski et al., 2020; Osinski et al., 2022, and references therein).

Impact crater formation comprises three main stages: contact and compression, excavation, and modification. Crater formation begins with the initial contact and compression stage when the impactor contacts the target surface and ends when the shock compression of the impactor completely dissipates. During the excavation stage, a mixture of fragmented target rocks with variable proportions of impact melt is ejected beyond the crater rim to form a continuous ejecta blanket (Osinski, 2004; Osinski et al., 2015; Mader and Osinski, 2018). The melt and fragmented target rock mixture derived from beneath the point of impact is deflected upward and outward parallel to the base of the transient cavity. This material remains in the transient cavity through the modification stage (Osinski et al., 2018; Osinski et al., 2022). Finally, the cratering process leaves sedimentary accommodation space. Simple hypervelocity impact craters comprise a bowl-shaped cavity with an uplifted and commonly overturned rim that approximately represents the transient cavity rim.

Lakes caused by an impact become infilled with sediments, which record post-impact craters and environmental changes. Lake sediments are important archives of climatic and environmental changes (Moscariello et al., 2000; Jin et al., 2009; Melles et al., 2011; Wennrich et al., 2014; Ebinghaus et al., 2017; Hagemans et al., 2021). Past lake environments have been characterized by investigating their sedimentary structures and facies (Nelson et al., 1986; Kerr et al., 1993; Masaitis, 2005; Osinski and Lee, 2005; Juschus et al., 2011; Zolitschka et al., 2015; Ebinghaus et al., 2017; Marcolla et al., 2021). This study investigated sediments in the impact crater of the Hapcheon Basin in the Republic of Korea. Our results provide new insights into the impact crater and its sedimentary history.

2 Geological setting and study site

The study area is located on the southern–central Korean Peninsula and is an impact crater formed by a meteorite impact (Figure 1A). The basin formed by the meteorite impact is surrounded by a mountain range (Figures 1B, C) and is only connected to adjacent areas by a river in the north. The Hapcheon Basin is a Cretaceous basin that contains terrestrial sedimentary and igneous rocks (Chough and Sohn, 2010). The Gyeongsang Basin was initially formed by NNE–SSW-trending faults and dipped 10°–15°E (Cheon et al., 2020). The Dongmyeong Formation occurs in the area surrounding the Hapcheon Basin and consists of sandstone interbedded with dark gray shale that was mainly deposited in a fluviolacustrine environment. The shale deposits contain numerous fossils and dinosaur footprints. Sandstone was deposited in distributary channels and delta lobe settings.

The 20HCL04 drill site is 21 m above the mean sea level (Figure 1C). In addition, a topographically well developed alluvial fan sedimentary layer exists in the Hapcheon Basin, and the alluvial fan topographical surfaces were classified into 3 categories: relatively high altitude, middle altitude, and low altitude (Hwang and Yoon, 2016). The 20HCL04 drill site is located in the middle alluvial fan system (Figures 1B, C) and is 1.35 km northwest of the 20CR05 drill site (Figure 1D) (Lim et al., 2021).

3 Methods

Drilling was undertaken with a truck-mounted drill rig and a wireline rotary coring system (5 cm in diameter). Sediment core recovery was >99% over the 66 m depth of the core (Supplementary Figure S1). Preliminary stratigraphic descriptions of the cores were made in the field. Subsequently, the cores were described in the laboratory and photographed.

X-ray computed tomography (CT) of the archived half of the core was undertaken using a medical CT scanner (Optima CT660) at the Korea Institute of Geoscience and Mineral Resources (KIGAM), Daejeon, Republic of Korea. The core was recovered from the MTD units with power settings of 120 kV and 160 mA (0.625 mm slices). The CT images were acquired for 1-m-long core samples from depths of 9–45 m (Supplementary Figure S2).

Ten organic samples collected from the core were used for radiocarbon dating. The radiocarbon dating samples were chemically processed using the acid–alkali–acid (AAA) method at the KIGAM Particle Accelerator Analysis (AMS) Center (Lee et al., 2000). Using an elemental analyzer, graphite was produced by CO_2 reduction and then used for radiocarbon dating (Hong et al., 2010).

Optically stimulated luminescence (OSL) dating was undertaken at KIGAM using samples collected from five depths in the core. For the dating of fine-grained samples, chemically purified quartz grains of 4–11 μm in diameter were extracted using sodium pyrophosphate ($Na_4P_2O_7{\cdot}10H_2O$) to remove any clay and hydrochloric acid (HCl) and hydrogen peroxide (H_2O_2) to remove any carbonate and organic matter, respectively. Finally, the samples were etched in H_2SiF_6 for chemical removal (Roberts, 2007; Kim et al., 2012). The separated quartz particles were analyzed at the KIGAM OSL laboratory.

Burial age dating using ^{26}Al and ^{10}Be is well-established and widely utilized as a rational and accurate method of radioisotopic dating (Granger et al., 1997; Granger and Muzikar, 2001; Balco and Shuster, 2009; Fujioka et al., 2009; Granger, 2014; Tu et al., 2015; Lebatard et al., 2019; Wang et al., 2019; Shaar et al., 2021). Burial

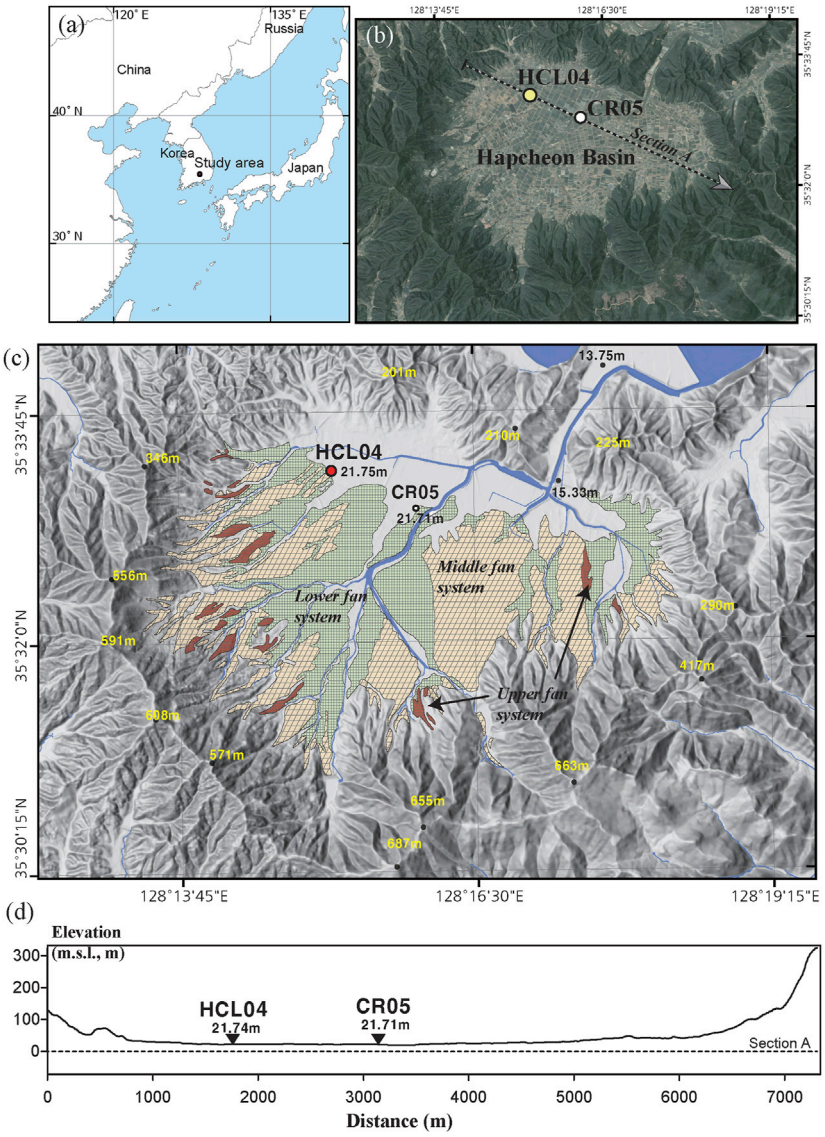

FIGURE 1
(A) Location map of the Hapcheon Basin. **(B)** The location of the cross-section and drill sites 20HCL04 and 20CR01 was reported by Lim et al. (2021). **(C)** Three types of alluvial fan systems were reported in the geomorphological study by Hwang and Yoon (2016). **(D)** Cross section showing the drill core location.

dating is based on the accumulation and radioactive decay of cosmogenic ^{26}Al and ^{10}Be, first exposed at the surface and then deeply buried (Granger and Muzikar, 2001; Granger, 2014). Simple burial dating relies on the assumption that post-burial production is negligible. Therefore, it is best suited for samples that are deeply and quickly buried, such as core samples. Two samples with sufficiently coarse quartz particles were taken from the core at 17.5 and 63.5 m depth to perform simple ^{26}Al/^{10}Be burial dating to determine the age of core samples. Each sample was subjected to sieving and hydrofluoric acid treatment to extract quartz grains from 300 to 500 g of soil samples. The chemical pretreatment procedure for measuring ^{10}Be and ^{26}Al contained in the sample was based on Kohl and Nishiizumi (1992). The sample was crushed to 150–355 μm, and organic materials and carbonates were removed using HCl–H_2O_2. The HF–HNO_3 leaching process (concentration of 1%–5%) was repeated three times in a high-temperature (~80°C) ultrasonic generator for 9 h to obtain the quartz grains from which meteoric ^{10}Be was removed. During the HF–HNO_3 pretreatment, magnetic and gravity separations were also conducted to separate the quartz from contaminants. The total Al concentration (<100 ppm) of the quartz grains was measured by inductively coupled plasma optical emission spectrometry (ICP-OES) in KIGAM with an uncertainty of 2%. Be and Al were separated and purified by ion chromatography. For the ^{10}Be/^{9}Be and ^{26}Al/^{27}Al measurements, BeO and Al_2O_3 target samples were analyzed in the accelerator mass spectrometry (AMS) facility operated by the Korea Institute of Science and Technology (KIST; Seoul, Republic of Korea) and calibrated using the methods of Nishiizumi et al. (2007) (^{10}Be) and Nishiizumi (2004) (^{26}Al). The results were calculated under the following assumptions: steady-state erosion. The

TABLE 1 Summary of sedimentary facies in the Hapcheon Basin.

	Facies	Characteristics (Description)	Interpretation
Gravel class	Densely packed sandy gravel facies (Gs1)	Predominantly clast-rich dense gravel with sand-dominant matrix, occurrence of various size impactite with muddy sand, and sub-rounded to sub-angular clasts	High-density flow dominated
	Sandy gravel and gravely sand facies (Gs2)	Loosely disorganized gravel with a sand-dominant matrix and clasts consists of sub-angular or sub-rounded clasts and occasionally displays upward-fining, but is mostly uniform	Subaqueous, high-density flow dominated
	Densely packed muddy gravel facies (Gm1)	Predominantly clast-rich, dense gravel with a mud-dominant matrix and sub-rounded to angular clasts	Debris flow dominated
	Muddy gravel and gravely mud facies (Gm2)	Loosely disorganized gravel with a mud-dominant matrix, clasts are angular or rounded, and occasionally display upward-coarsening, but mostly uniform	Subaqueous debris flow dominated
Sand class	Massive sand facies (Sm)	Interbedded, gray with occasional angular gravel clasts; sub-rounded to well-rounded coarse sand of a light gray color; and medium-to-coarse-grain sand, relatively well sorted and partly reddish and brownish in color	Stream or channel within fluvial flow dominated
	Liner interbedded sand facies (Sl)	Linear interbedded structure in the coarse sand layer; intercalated 1–5 cm thin-bedded silty sand; partly slightly clast fabric; and fining-upward, but mostly uniform	Channel bar within fluvial flow dominated
Mud class	Massive mud facies (Mm)	Massive, homogeneous, and non-laminated silty mud; and occasionally bioturbated and organically rich, fining-upward	Suspended sedimentation dominated
	Laminated mud and sandy mud facies (Ml)	Rhythmically intercalated mud, thin-bedded silty mud, olive-gray in color, with very fine sand, sheet-like distribution, and organic matter (plant materials) in individual beds	Suspended sedimentation dominated
	Deformed mud and sandy mud facies (Md)	Irregularly bedded and a massive laminated layer deformed such as having a wavy, convoluted, and folded shape	Slide and slump processed after deposition
	Mud with tephra glasses facies (Mt)	Pinkish light to medium gray thin-interbedded 6-cm thick silty mud, pinkish gray in color, and very fine sand separated by thin silt layers	Volcanic transport dominated

measured isotope concentrations were corrected to the production rate in the study area based on the production rate of the sea level high latitude (SLHL) (Stone, 2000). Simple burial ages were calculated using the simple burial age method described by Granger and Muzikar (2001) and Granger et al. (2013).

Grain size analysis was performed using conventional sieving methods (>2 mm; wet sieving, drying, and weighing) and laser particle size (LPS) analysis (<2 mm fraction) on 120 samples. Hydrogen peroxide (10%) was used to remove organic matter from dry samples (300 mg), and 1 N hydrochloric acid was used to remove carbonates and iron oxides. After pre-processing, the samples were analyzed using a Mastersizer 3000 laser analyzer (Malvern Instruments Limited, UK).

4 Results

4.1 Sedimentary facies

Ten distinct sedimentary facies were identified from the sedimentary textures and structures based on photographs, CT images, and grain size data.

4.1.1 Clast-supported sandy gravel (Gs1) facies

4.1.1.1 Description

The densely packed sandy gravel (Gs1) sedimentary facies is characterized by clast-supported granular to cobble-sized material (Table 1) (Figure 2; 65–66 m; Figure 3; 13–14 and 10–11 m). Pebbles that are 3 cm in size dominate, but 5 cm-sized cobbles were occasionally observed. Gs1 is poorly sorted, and the clasts are not oriented. The clasts consist mainly of sedimentary rocks and are predominantly angular, with some subrounded-to-subangular clasts. The matrix consists of coarse to medium-grained, dark gray to gray sand. The clasts are sandstone and mudstone from the basement sedimentary rocks. This gravel bed is commonly observed in the core from 51 to 66 m depth. Sediments related to impact cratering (impactites) also occur in Gs1, including impact melt breccias and melted rock fragments (Figures 5C–F) (Osinski, 2003, Osinski, 2004; Osinski et al., 2015; Osinski et al., 2018; Osinski et al., 2022).

4.1.1.2 Interpretation

Gs1 occurs mainly in the lower part of the core. This tightly packed gravel layer at 64–65 m depth is interpreted as a debris flow and hyper-concentrated sediment flow deposit, although some of this facies may have been formed by rock avalanche deposition. Because the coarse clasts and sandy matrix indicate high-energy flow regimes, Gs1 is interpreted to have formed in a stream-dominated alluvial fan setting (Ridgway and Decelles, 1993).

4.1.2 Matrix-supported sandy gravel and gravelly sand (Gs2) facies

4.1.2.1 Description

The pebble-bearing sandy gravel and gravelly sand (Gs2) facies consists of matrix-supported gravel-to-cobble-sized material (Figure 1; 59–62 m; Figure 3; 13–14 and 10–11 m). The clasts are mainly 4 cm in size, but 10 cm-sized cobbles were rarely observed. Gs2 is very poorly sorted. The clasts are

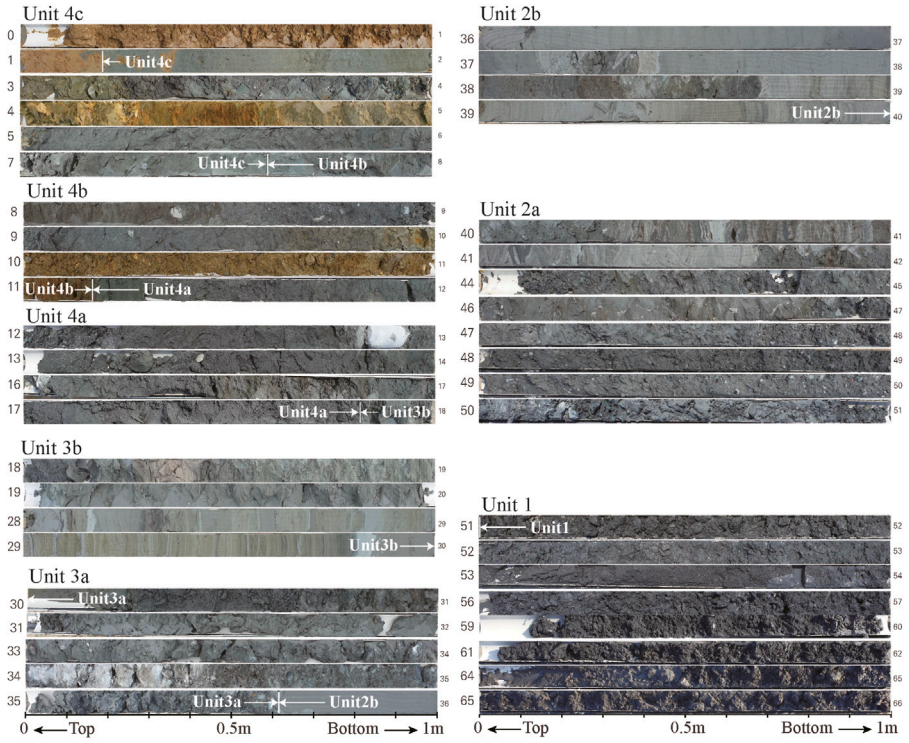

FIGURE 2
Selected photographs of samples from drill core 20HCL04. The scale is 1 m and subdivided into 10 cm.

primarily sedimentary rocks and angular, with some angular–subangular clasts. Some clasts are impactites. The matrix consists of coarse-to-medium-grained sand. This facies is generally ~1 m thick but can be >2 m. Some parts of Gs2 exhibit weak horizontal stratification and rapid upward fining. Some parts of this facies also exhibit weak normal to reverse grading. Gs2 is interbedded with massive sand (Sm), planar interbedded sand (Sl), and densely packed sandy gravel (Gs1).

4.1.2.2 Interpretation

Gs2 is interpreted to have been deposited by stream flow in an alluvial fan or by a debris flow, and it transitions into the Gs1 facies where it exhibits normal to reverse grading typical of subaqueous alluvial fan deposits formed by debris (Ridgway and Decelles, 1993) and hyper-concentrated grain (Miall, 2006) flows.

4.1.3 Clast-supported muddy gravel (Gm1) facies

4.1.3.1 Description

The densely packed muddy gravel (Gm1) facies consists of a clast-supported gravel-to-cobble-sized material (Figure 3; 44–45, 35–36, and 34–35 m). It contains mainly 1.5-cm-sized pebbles, but some 8-cm-sized cobbles were occasionally observed, for example, at depths of 35.0–35.6 m (Figures 3D, E). Gm1 is very poorly sorted. The clasts consist of sedimentary rock, are predominantly angular and subangular, and have variable colors. The matrix consists of (brownish) gray silty to sandy mud. Gm1 contains unoriented clasts, but a weak horizontal fabric occurs at 11.4–11.6 m depth (Figures 3B, E, N).

4.1.3.2 Interpretation

The low matrix content (e.g., 35.5–35.6 m depth), sharp lower contact, and unoriented gravel to pebble clasts indicate deposition from viscous gravelly debris or hyper-concentrated flows (Maharjan et al., 1970; Horton and Schmitt, 1996; Yu et al., 2019). The Gm1 facies was deposited by a debris flow. Hyper-concentrated sediment flows occur in subaerial environments, such as alluvial fans, slope aprons, and rock avalanches, or as high-density turbidite flows in subaqueous environments (Nelson et al., 1986; Ineson, 1989; Kim and Chough, 2000; Pope et al., 2008; Li et al., 2016). Based on the morphology of a simple impact crater (Osinski et al., 2022, and references therein), water sources are limited to the drainage area from the crater rim wall. Therefore, the sedimentary sources of debris flows and rock avalanches were deposited in the proximal area of an alluvial fan adjacent to the crater lake.

4.1.4 Matrix-supported muddy gravel and gravelly mud (Gm2) facies

4.1.4.1 Description

The pebble-bearing muddy gravel and gravelly mud (Gm2) facies is a disorganized, matrix-supported gravel containing mainly subrounded-to-subangular, 2-cm-sized pebbles, although 10-cm-sized cobbles were rarely observed (Figure 3; 44–45, 42–43, 40–41, 35–36, 34–35, and 11–12 m). Gm2 is very poorly sorted, and the clasts primarily consist of sandstones, mudstones, and rare impactites. The matrix is a mixed sand and silt-rich mud, that is light-to-dark gray in color. The clasts in Gm2 exhibit normal-

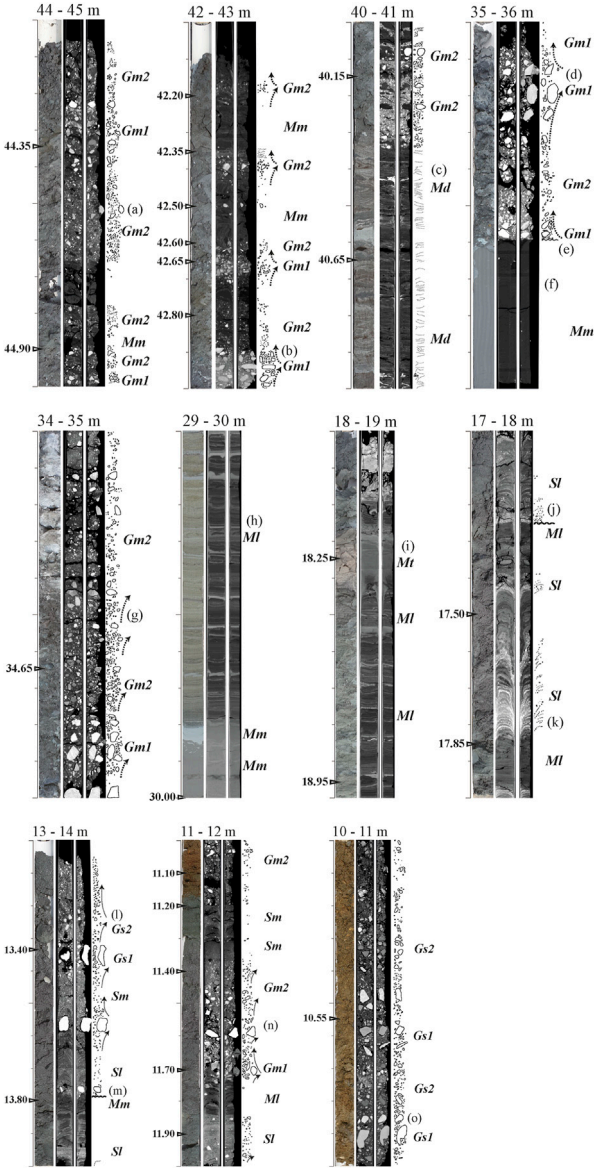

FIGURE 3
Selected photomicrographs and three-dimensional X-ray computed tomography (CT) images of typical sedimentary facies in the 20HCL04 drill core samples. Each sub-figure consists of a photograph, a horizontal two-dimensional X-ray CT image, and a vertical two-dimensional X-ray image at the same depth. Facies are indicated in italics and bold: Gs1, densely packed sandy gravel facies; Gs2, sandy gravel, and gravelly sand facies; Gm1, densely packed muddy gravel facies; Gm2, muddy gravel, and gravelly mud facies; Sm, massive sand facies; Sl, planar interbedded sand facies; Mm, massive mud facies; Ml, laminated mud and sandy mud facies; Md, deformed mud and sandy mud facies; Mt, mud and tephra facies. Unconformities are shown as wavy lines and sediment grading is shown by arrows. Typical structures in each facies are annotated **(A–O)**.

to-inverse grading or are not graded (Figure 3; 42–43, 35–36, 34–35, and 13–14 m). Grading is also observed in the matrix.

4.1.4.2 Interpretation

Gm2 has a high matrix content and unoriented clasts (Figure 3A), indicating deposition in viscous gravelly debris flow channels that may have been mass flows. Normal grading or normal-to-inverse grading is interpreted to reflect changes in flow regime in a subaerial or subaqueous environment (Heward, 1978; Shultz, 1984; Sletten et al., 2003; Fanetti et al., 2008; Talling et al., 2012). The grading of the matrix and clasts in Gm2 is interpreted to be due to hyper-concentrated flow deposition, given that a hyper-concentrated suspension has a weak yield strength and becomes density-stratified. Gm2 could have been deposited as a high-energy debris flow or by bedload transport in the laminar-to-turbulent flow regime (Miall, 2006). However, in this case, Gm2 may also have been deposited by the migration of gravel sheets across bar tops or by the development of fan lobes (Tha et al., 2015).

4.1.5 Massive sand (Sm) facies

4.1.5.1 Description

The massive sand (Sm) facies consists of fine-to-medium-grained sand with sparse pebbles. It is well-sorted and common

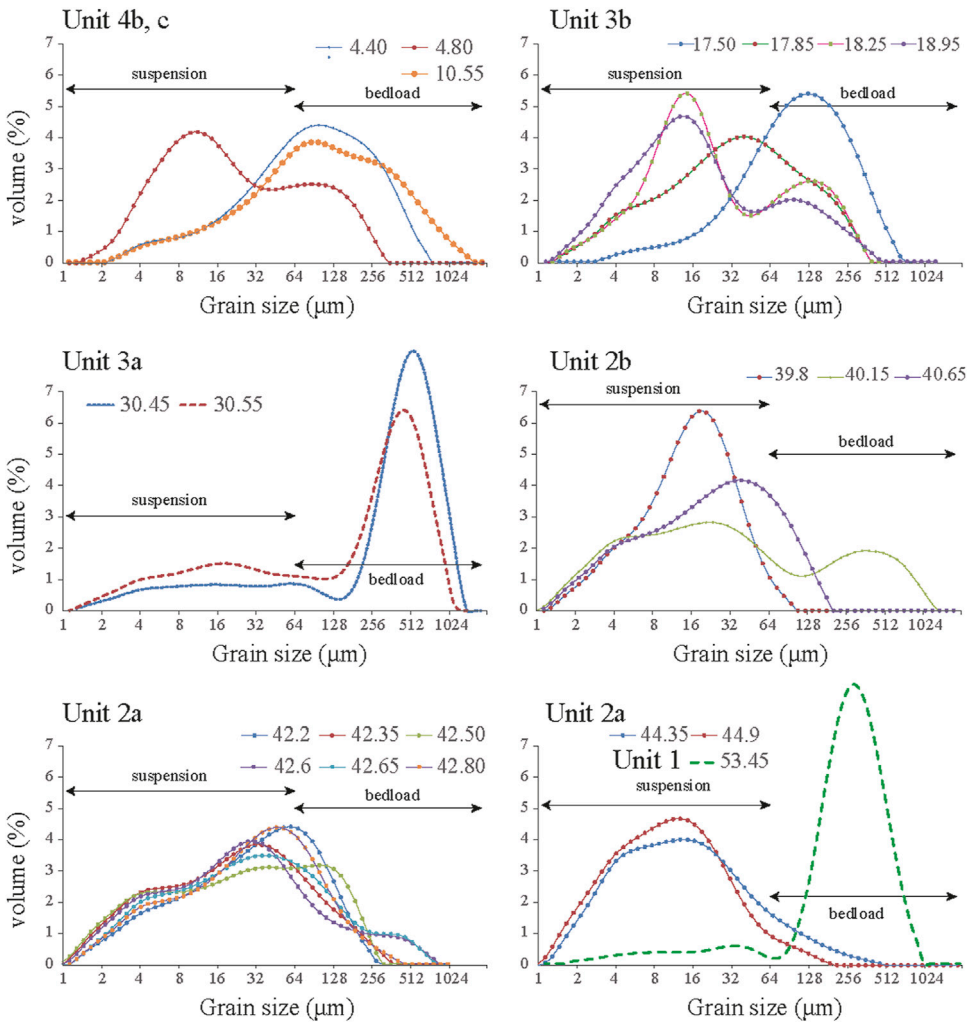

FIGURE 4
Grain size distribution plots for selected sediment samples. The scale is $\log_{10}$ (2 mm).

in the gravel layers. The Sm facies occurs at 11.85–12.0, 30.3–30.6, and 53.3–53.6 m depth (Figures 2, 4; 53.45, 30.45, and 30.55 m depth; Figure 3; 13–14 and 11–12 m depth). Sm occurs mainly between the lower and upper parts of Gs2 and is generally 10–20 cm in thickness. Internal structures are not present, distinguishing Sm from the planar interbedded and graded sand (Sl) facies. Massive brownish sand occurs at 10.0–11.2 m depths (Figure 3).

4.1.5.2 Interpretation

Sm is massive and well-sorted sand and is interpreted to have been deposited by bedload or as basal fill-in channels (Miall, 2006). The massive brownish sand, including some gravel, is interpreted to have been subaerially exposed, which caused oxidization.

4.1.6 Planar interbedded and graded sand (Sl) facies

4.1.6.1 Description

The planar interbedded sand (Sl) facies is coarse-to-medium-grained sand, poorly sorted, and light gray in color. The Sl layers at 38.5–38.7 and 17.6–17.8 m depths occur only as lenses in CT images (Figure 3; 17–18, 13–14, and 10–11 m), as Sl is poorly preserved in the drill core. Locally, Sl overlies small-scale, cross-laminated sand. Sl is massive or diffusely graded, weakly planar-bedded, and typically occurs at 39.2–39.3 and 17.45–17.5 m depths. Sl exhibits fining-upward, erosive bases, and small-scale interbeds with silty sand. Sl occurs mainly between the lower and upper parts of Gs2 and is generally 10–20 cm thick.

4.1.6.2 Interpretation

Sl facies exhibits horizontal and cross-bedding, reflecting the intermingling of distributary channels in a fluvial and alluvial setting on a subaqueous platform (Alván and von Eynatten, 2014; Gao et al., 2019; Winsemann et al., 2022). The stratified sand beds record the accretion and downstream migration of bar forms, with the coarsening-upward trend indicating downstream armoring. These bar forms have features typical of mid-channel or longitudinal bars (Kostaschuk et al., 1986; Nemec and Postma, 1993; Ridgway and Decelles, 1993).

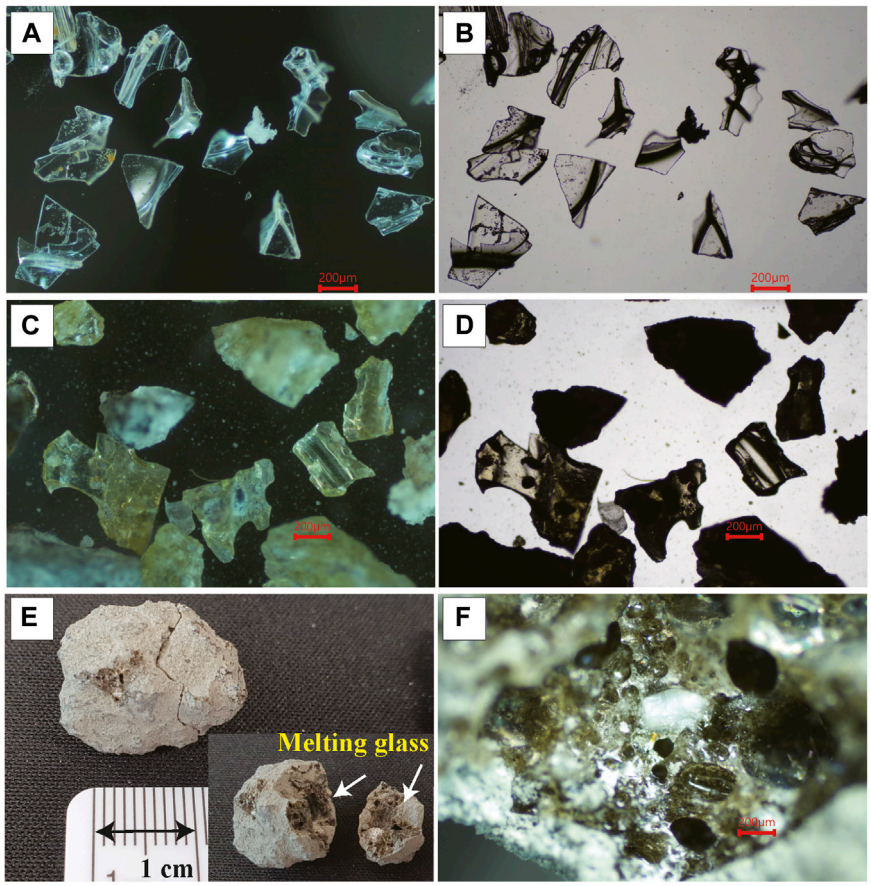

FIGURE 5
Photomicrographs of typical sediments from core 20HCL04. **(A–B)** Photomicrographs of tephra shards extracted from the sediment samples at 18.4 m depth (A, stereo-image; B, composite image). Shards are white in color and have platy, cuspate, and pumiceous morphologies. **(C–D)** Photomicrographs of tephra shards and fragments of melt rocks extracted from the sediment samples at 63.85 m depth (C, stereo-image; D, composite image). Shards are white or yellow in color and have platy, cuspate, and vesicular morphologies. **(E)** Photomicrograph of melt breccia sampled at 51.97 m depth, which shows two fragments of melt glass (indicated by the arrows). **(F)** Photomicrographs of melted glass fragments. Scale bars are 200 μm in length.

4.1.7 Massive mud (Mm) facies

4.1.7.1 Description

The massive mud (Mm) facies comprises fine to very fine sandy to silty mud. The lower part is dominated by sandy mud and the upper part by mud (Figure 3; 44–45, 42–43, 35–36, 29–30, and 13–14 m), and weak normal grading is evident. Individual layers of Mm are very thin (5–20 cm) and interbedded with gray mud. Rare angular to subangular granules occur in this facies. Scattered organic materials are also present but are not abundant. The top and bottom of Mm are in abrupt contact with other lithofacies, such as Ml and Sm.

4.1.7.2 Interpretation

Mm occurs mainly between the lower and upper parts of Gm2 and is generally 10–20 cm in thickness. The Mm facies is widespread in the deep lacustrine sediments. Normal grading is typical of turbidite sediments (Ineson, 1989; Bouma, 2000; Mulder and Alexander, 2001; Yu et al., 2019), and thus Mm records a weakening of the flow energy during deposition. Sandy debris flows mix extensively with water in deep lake environments, leading to a further reduction in fluid density, which leads to turbulently supported sediment flows (Li et al., 2016).

4.1.8 Laminated mud and sandy mud (Ml) facies

4.1.8.1 Description

The laminated mud (Ml) facies consists of planar bedded mud (Figure 3; 29–30, 18–19, 17–18, and 11–12 m). It is generally ~0.5 m thick and most abundant at 17.8–30 m depth. Organic matter occurs in the upper part of this facies but is not abundant. Laminations of variable thickness are well-developed, and the sedimentary structure is mainly defined by color and grain size (Figure 3, 29–30 m; Figure 4B, 18.95 m). Laminations consist of alternating massive mud (Mm) facies in brown, gray, and white colors. The laminated mud layers have sharp planar contacts, although these are less distinct in some intervals. The laminae are commonly >1 mm thick. The laminated mud layers consist mainly of silt and <5% clay (Figure 6).

4.1.8.2 Interpretation

The fine-grained and generally well-sorted nature of Ml indicates that this facies was mainly deposited from suspension

in stagnant or slow-moving waters, probably in a lake or swamp setting (Miall, 2006).

4.1.9 Deformed mud and sandy mud (Md) facies

4.1.9.1 Description

The deformed mud and sandy mud (Md) facies comprises alternating green–gray silty mud and gray silty mud. This facies was initially deposited as the Ml facies. The Md facies exhibits deformation structures, such as folding, convoluted, and zig-zag bedding (Figure 3C, 40–41 m). The Md sediments may have been reworked. The convoluted, folded bedding and distorted thin mud beds are interbedded with Gm2, with the latter being a poorly sorted mixture of pebble-to-cobble-sized clasts set in a muddy matrix.

4.1.9.2 Interpretation

The Md facies is a secondary unit formed from previously deposited muddy sediments. The Hapcheon Basin is located within a major fault system (i.e., the Yangsan Fault) on the eastern side of the Korean Peninsula (Cheon et al., 2019). Therefore, post-depositional deformation was likely caused by large rainfall events and seismic activity. The soft sediment deformation structures of Md may be related to earthquake events (Jiang et al., 2016; Rana et al., 2016; Tinterri et al., 2016; Gao et al., 2020). In addition, a slump-like structure was observed.

4.1.10 Mud and tephra (Mt) facies

4.1.10.1 Description

The mud and tephra (Mt) facies has a light pink color and is 10-cm-thick, silt-bearing, thin-bedded sand that clearly contains tephra (Figure 3, 18–19 m; Figure 4B, 18.25 m). The silt-sized grains of tephra do not include other reworked sediments. This facies is rarely laminated and consists mainly of volcanic glass (Figures 5A, B).

4.1.10.2 Interpretation

Mt is ash deposited from a volcanic eruption either nearby on the Korean Peninsula (Chun and Cheong, 2020; McLean et al., 2020; Chen et al., 2022) or in another country, such as Japan (Machida, 1999; Ikehara, 2015; Matsu'ura et al., 2017).

4.2 Sedimentary environments

Four sedimentary units and eight sub-units were classified into units 1–4 from the base to the top of the core (Figure 3). The main characteristics and sedimentary facies are detailed in Table 3.

4.2.1 Unit 1: distal margin of subaqueous alluvial fan–delta

The Gs1, Sm, and Gs2 facies occur in Unit 1. The gravel clasts in Unit 1 are sandstone and mudstone from the sedimentary bedrock, and Unit 1 has relatively high contents of melt breccia and melt rock fragments compared to the upper units (Figures 5C–F). This high content of melt rocks from the crater wall and fallback material marks the onset of sedimentation in the crater.

Unit 1 is characterized by normally graded, sandy–pebbly gravels that alternate with massive coarse sand. Given the bowl-shaped topography formed by meteorite collisions (Osinski et al., 2022, and references therein), the sediment supplied from the steep crater wall was carried by debris flows, which produced various sediment types depending on water content. Gs1 and Gs2 in Unit 1 are dark gray in color and do not have defined contacts. The underlying gravel exhibits normal grading typical of alluvial fan deposits. Gs1 and Gs2 are typical debris flow deposits formed in a subaqueous alluvial fan–delta (Al-Sarawi, 1988; Francke et al., 2016; Ebinghaus et al., 2017; Ye et al., 2021). The uppermost 10 cm of Unit 1 comprises highly packed clasts that are in unconformable contact with Unit 2.

4.2.2 Unit 2: alluvial fan (Unit 2a) and shallow lake (Unit 2b)

Unit 2 is subdivided into Units 2a and 2b. The Gm1, Gm2, Sm, Sl, Mm, and Ml facies occur in Unit 2a, and the Gm2, Sm, Sl, Mm, Md, and Ml facies occur in Unit 2b. Unit 2 is characterized by a fining-upward sequence and repeated couplets of lower gravel and upper mud facies (Figure 3). This is important evidence for multiple sedimentary sources from a slope apron system (Nelson et al., 1986; Li et al., 2016). Units 2 and 3 are clearly distinguished from Units 4 and 1 by the muddy matrix (Figure 5) of the former. Gravel in Unit 2 is relatively fine-grained compared to Unit 1. Unit 2a is interpreted to have been deposited in a subaqueous environment, in which middle fan–delta and high-density flow deposits are interbedded. In contrast, Unit 2b is interpreted to have been deposited in a shallow-water lake. Horizontal laminae and bedding developed on top of the dark gray mud on top of the gravelly mud, indicating that these sediments were deposited by hyper-density flows and turbidity currents (Maharjan et al., 1970; Heward, 1978; Miall, 2006; Talling et al., 2012).

Unit 2 records frequent environmental changes. The Gm1 and Gm2 facies repeatedly exhibit reverse grading (Figure 3). In particular, these facies exhibit characteristics of alluvial fan deposits formed by hyper-concentrated and debris flows in a subaqueous environment. As a consequence of their high-relief catchments, alluvial fans tend to aggrade by catastrophic sedimentary processes associated with occasional flash flood events of relatively short duration and by debris flows with high sediment-to-water ratios (Heward, 1978; Shultz, 1984; Sletten et al., 2003; Fanetti et al., 2008; Talling et al., 2012).

4.2.3 Unit 3: alluvial fan (Unit 3a) and deep lake (Unit 3b)

Unit 3 is subdivided into Units 3a and 3b. The Gm1, Gm2, Sm, Sl, Mm, and Ml facies occur in Unit 3a, and the Sm, Sl, Mm, Ml, and Mt facies occur in Unit 3b. Like Unit 2, the matrix of Unit 3 consists of clay and exhibits characteristics typical of alluvial fan deposits formed by hyper-concentrated and debris flows in a subaqueous environment. Unit 3a is interpreted to have been deposited in a relatively deep, large-scale, central part of a subaqueous alluvial fan. In contrast, Unit 3b is interpreted to have been deposited in a deep lake. In Unit 3b, planar bedding and laminations are well-developed. These layers were likely generated by an event sequence, but they are unlikely to be varve sediments because they do not repeat rhythmically. Laminations and bedding may have been formed by surge events.

4.2.4 Unit 4: subaerial alluvial fan and fluvial channel

Unit 4 is subdivided into Units 4a, 4b, and 4c. The Gs1, Gm1, Gs2, Gm2, Sm, Mm, and Ml facies occur in Unit 4a; the Gs1, Gm1,

TABLE 2 Accelerator mass spectrometry (AMS)^{14}C age data for core 20HCL04. All dates were calibrated to calendar years before the present (cal. yr BP relative to 1950 AD) using the OxCal program with the INTCAL13 calibration dataset for plant fragments (Reimer et al., 2013).

Depth (m)	14C BP (±1 s)[a]	d^{13}C (‰)	d^{13}C error (‰)	Laboratory code	Dated material
4.74	<50,000[b]	−26.77	0.8	IWd210037	Plant materials
5.82	46,276 ± 711	−34.17	0.59	IWd210038	Plant materials
9.37	<50,000[b]	−27.90	0.5	IWd210039	Plant materials
16.62	<50,000[b]	−31.05	1.15	IWd210040	Plant materials
23.46	47,749 ± 823	−33.28	1.16	IWd210041	Plan materials
27.07	<50,000[b]	−31.80	1.19	IWd210042	Plant materials
28.31	<50,000[b]	−28.95	1.06	IWd210043	Plant materials
38.78	<50,000[b]	−28.75	0.88	IWd210044	Plant materials
40.63	<50,000[b]	−31.42	1.32	IWd210045	Plant materials
45.03	<50,000[b]	−25.31	1.09	IWd210046	Plant materials

[a]Libby^{14}C half-life (5,568 years). The quoted error on the BP date is 1 sigma (1 relative standard deviation with 68% probability) of counting error.
[b]Over the detection limit: 54,703 BP.

TABLE 3 Cosmogenic nuclide concentrations of two samples. The simple burial age of each sample was calculated (without post-burial production corrections) following the method of Granger and Muzikar (2001) and Granger et al. (2013). The simple burial ages are not the true burial ages.

Sample	Quartz mass (g)	^{10}Be (×10^5 at/g)	^{26}Al (×10^5 at/g)	^{26}Al/^{10}Be	Burial age (Ma)
HCL04 17.5 m	30.5	12.35 ± 0.418	57.55 ± 5.21	4.66 ± 0.41	0.52 ± 0.17
HCL04 65.0 m	31.2	6.91 ± 0.228	22.17 ± 1.54	3.21 ± 0.23	1.33 ± 0.14

[a]Standards and analytical procedures are detailed in the text.
[b]Burial ages were calculated following the procedure for simple burial dating outlined by Granger and Muzikar (2001) and Granger (2014). Radioactive half-life values of 1.387 ± 0.012 Myr for ^{10}Be (Chmeleff et al., 2010) and 7.17 ± 0.17 × 10^5 years for 26Al (Granger, 2006) were used.
[c]The ^{10}Be/^{9}Be ratio in the blanks was 7.66 ± 1.3 ×10^{-15} and the ^{26}Al/^{27}Al blank ratio was 3.5 ± 4 ×10^{-15} for the initial measurement.

Gs2, Sm, Sl, and Mm facies occur in Unit 4b; and the Gs1, Gs2, Sm, and Sl facies occur in Unit 4c.

The lower part of Unit 4a represents a gradual transition from Unit 3b and, thus, a gradual change in the depositional environment. Although the lake setting persisted after the deposition of the Mt facies in Unit 3b, the environment of the subaerial alluvial fan and high-density flows became dominant, with sediments supplied from adjacent slopes. Channel bodies along the bars were filled with upward-fining sand and mud, indicating bed aggradation, channel obstruction, and local avulsion (Heller and Paola, 1996). Unit 4b represents clast-to-matrix-supported, fine upward surge deposits. More compacted and coarser clast-supported gravels (Gs1 and Gm1 facies) and fine-grained layers (Gm2 and Mm facies) indicate more high-energy depositional events during the deposition of the uppermost part.

Scattered, clast-supported deposits in Unit 4c (Figure 3) suggest that exceptional, high-energy events occurred or that the deposits were entirely reworked based on the occurrence of unoriented angular clasts. The basal surfaces of Unit 4c are distinct and marked by pebble-to-cobble-sized clasts.

4.3 Ages of Units 3 and 1

The plant fragments sampled at depths of 5.82 and 23.46 m in core 20HCL04 yielded radiocarbon ages of 46,000 and 48,000 cal. yr BP, respectively. In addition, the measured radiocarbon age was actually at the limit of detection and was considered a minimum age. The other radiocarbon ages were >50,000 cal. yr BP and beyond the radiocarbon dating limit (Table 2). Two fine-grained (4–11 μm) quartz OSL samples were collected from core depths of 5.5 and 7.5 m in core 20HCL04, with De values of 545 ± 33 Gy and 552 ± 34 Gy, respectively. However, the 2*D0 values of the exponential component were observed to be 459 ± 16 Gy and 491 ± 24 Gy, respectively. When De is greater than twice D0, De values should not be calculated because of the dose characterizing the rate of signal increase within the saturating exponential (Wintle and Murray, 2006; Kim et al., 2010). Therefore, the De values of two OSL samples were obtained in a dose range where the exponential component was saturated.

Simple burial dating derived from ^{26}Al and ^{10}Be measurements of core samples at depths of 17.5 m and 63.5 m were observed to be 0.52 ± 0.17 and 1.33 ± 0.14 Ma, respectively (Table 3). Ages were based on two basic assumptions. First, and most importantly, we calculated burial ages by assuming either negligible or steady-state erosion. Post-depositional nuclide production was not considered. The quartz minerals must have undergone only one exposure–burial cycle in the past *ca.* 10 Myr to satisfy this assumption. If this assumption is incorrect, then the burial age must be considered the maximum. The

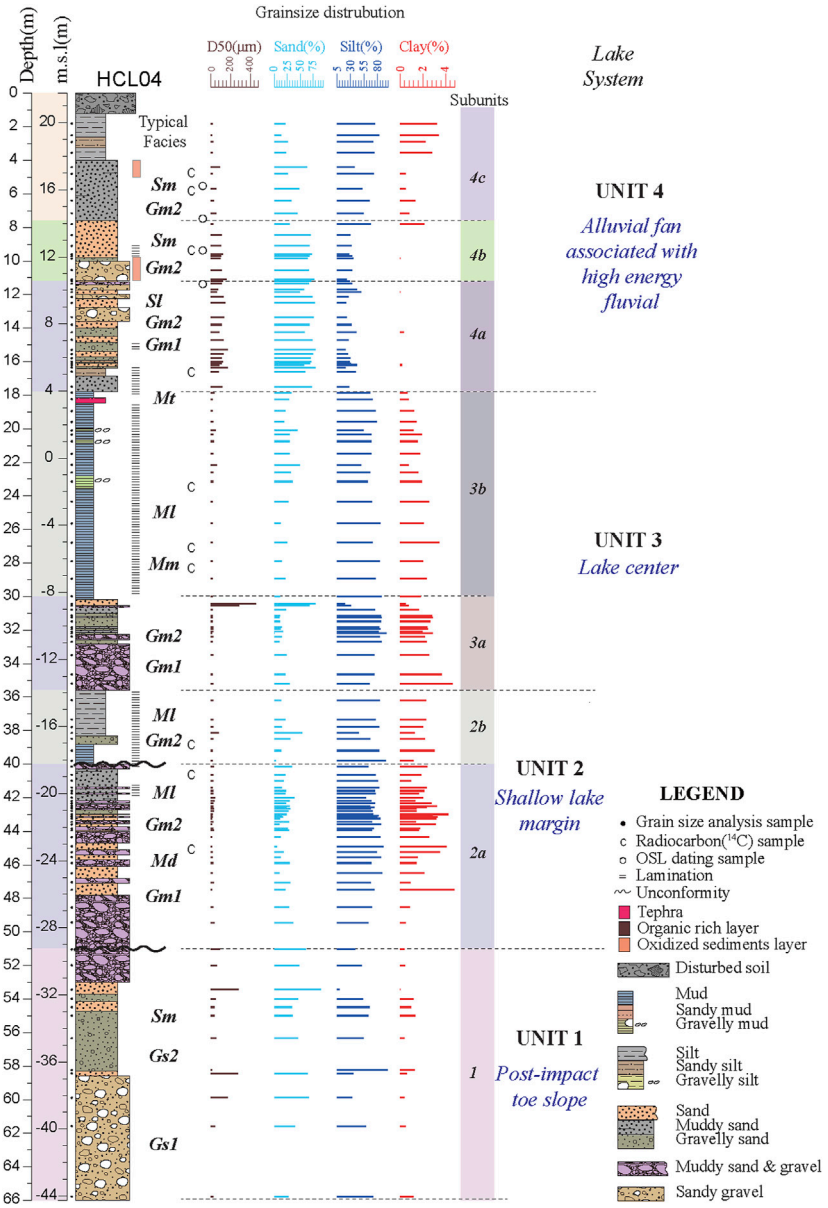

FIGURE 6
Stratigraphy of drill core 20HCL04 showing the lithologies, interpreted sedimentary units and facies, ^{14}C ages (C symbols), OSL ages (O symbols), and grain size (clay, silt, and sand in percent). Dominant facies are indicated in italics and bold: Gs1, densely packed sandy gravel facies; Gs2, sandy gravel, and gravelly sand facies; Gm1, densely packed muddy gravel facies; Gm2, muddy gravel, and gravelly mud facies; Sm, massive sand facies; Sl, planar interbedded sand facies; Mm, massive mud facies; Ml, laminated mud and sandy mud facies; Md, deformed mud and sandy mud facies; Mt, mud and tephra facies.

possibility that the two dated samples underwent a complex exposure–burial history cannot be ruled out. Second, the samples were assumed to have been buried at a sufficient depth to neglect the effects of cosmogenic nuclide generation, owing to post-burial muons. The two dated samples were obtained from deeply drilled cores, and the possibility of post-burial cosmogenic nuclide generation can be ruled out.

The ages of 1.33 ± 0.14 Ma at 63.5 m depth (Unit 1) and 0.52 ± 0.17 Ma at 17.5 m depth (Unit 3a) are thought to provide reliable age constraints on the studied core. Simple burial dates from the two samples are in stratigraphic order.

5 Discussion

5.1 Crater sedimentation and post-cratering evolution

The *ca.* 66-m-thick sediment core provided the first record of the syn-to-post-cratering of the Hapcheon impact crater. Sedimentation occurred in four depositional stages, as suggested by the vertical sequence of facies from Units 1 to 4 (Figure 6). The sedimentary environments represented by the 20HCL04 core are discussed in the following paragraph, with constraints provided by the previously reported

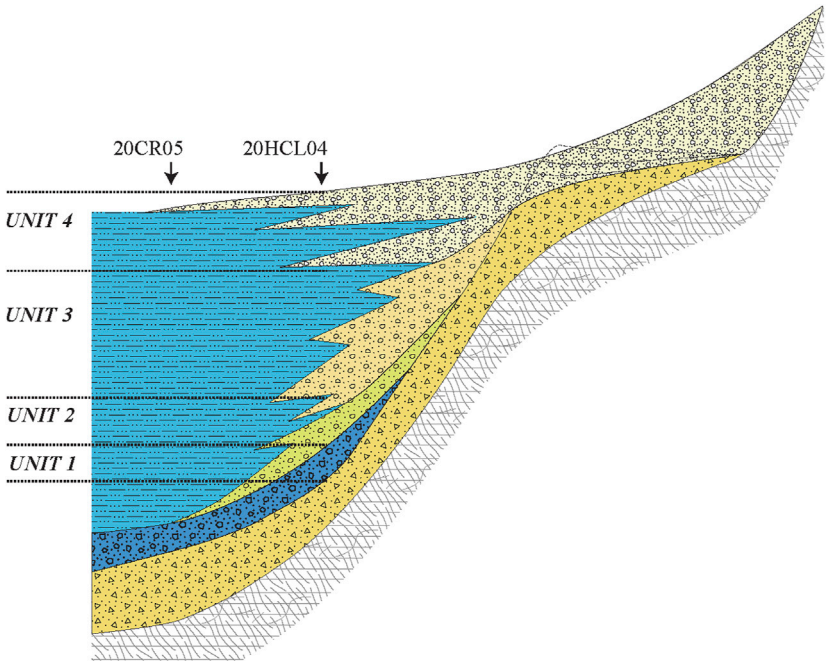

FIGURE 7
Schematic depositional model for the crater lake of the Hapcheon Basin, showing the alluvial fan and lacustrine systems and sedimentary units.

20CR05 core (Figure 7) (Lim et al., 2021). Considering existing studies showing that the permeability of rocks increases immediately after a meteorite collision, there is a clear possibility that groundwater can fill the empty lake formed after the impact (Parnell et al., 2010; Komatsu et al., 2014). However, more mineralogical evidence is needed to confirm groundwater inflow into the lake, and further research is necessary in this regard. Therefore, even if groundwater influenced the collision crater lake, there was no significant change in the sedimentary interpretation of the sediments flowing into the lake. As a result, changes in the sedimentary environment caused by groundwater were not considered separately in this study.

5.1.1 Deposition of Unit 1

The depositional record of Unit 1 is incomplete because of the limited core recovery from the expected base of the sediments (Figure 6). Based on the cratering process reported in a previous study, the initial crater floor before sediment infilling was a breccia layer or fractured basement rocks (Lim et al., 2021).

The 20HCL04 core did not recover the lowest part of the sediments in contact with the brecciated fracture zone, whereas the 20CR05 core did drill through these sediments. The Gs1 and Gs2 facies, consisting of mixed sand and gravel, were emplaced on the crater floor by gravity and overriding concentrated density flows. Angular gravel of country rock was observed to be mixed with melt breccia, fragments of melt rocks, and melt glass (i.e., fallback ash) related to the impact. The age of 1.33 ± 0.14 Ma dates the impact collision and the onset of sedimentation after the formation of the Hapcheon crater. This (before 63,000 yr. BP) is quite different from that reported by Lim et al. (2021).

This first depositional stage in the Hapcheon crater was characterized by the collapse of unstable crater walls and the re-deposition of unconsolidated ejecta and fallback tephra on steep slopes. Similar coarse-grained clastic deposits rich in wall-rock fragments occur in basal crater sediments elsewhere. The subaqueous emplacement of the basal coarse-grained clasts and the normal grading of Gs1 suggest that a body of water quickly began to accumulate in the post-impact stage.

The deposition of Unit 1 possibly occurred in the middle of an alluvial fan or a subaqueous alluvial fan–delta (Maharjan et al., 1970; Heward, 1978; Ghibaudo, 1992; Kim and Chough, 2000; Liu et al., 2019; Yu et al., 2019; Barrett et al., 2020). Common debris flow deposits are matrix-supported. The sediments of Unit 1 exhibit normal grading and are clast- and matrix-supported. Thus, the depositional environment is interpreted to have been in the middle of an alluvial fan, with the debris sources near the crater wall. Some of the sediments were transported using stream or channel flow processes (Sm) to the middle of the alluvial fan (Figure 7). The water source for transporting the sediments may have been the local watershed, climate-driven precipitation, or groundwater discharge.

5.1.2 Deposition of Unit 2

The deposition of Unit 2 was characterized by sediment with a finer-grained matrix compared to Unit 1 (Figure 6). The sedimentary facies in Unit 2 represent multiple alluvial processes and sediment sources with rapidly changing sedimentary environments (Figure 7).

Slope failures, such as landslides and rock avalanches from the crater walls, formed slope deposits with morphologies typical of a slope apron or alluvial fan (Yu et al., 2019; Yu et al., 2019), indicating that the crater had multiple sediment sources. Unit 2 had a sharp contact with Unit 1, and the matrix in Units 1 and 2 clearly changed from coarse to fine sand.

Unit 2 consists of subunits 2a and 2b. Unit 2a is characterized by clast-dominated sediments with a muddy matrix, and Unit 2b is characterized by a muddy matrix with rare clasts. Unit 2 is interpreted to have been deposited in an environment that transitioned from an alluvial and shallow-water setting to a deep-

water setting during the deposition of Unit 3. This transition can be attributed to various factors, such as climate change, tectonic setting, relative erodibility of the source rocks, and availability of surficial deposits within the drainage basin (Hooke and Rohrer, 1977; Ritter et al., 2000; Andrews and Hartley, 2015; Winsemann et al., 2022).

The sedimentary facies of Unit 2 exhibit many changes indicative of subaerial to subaqueous environments (Figures 6, 7). Normal grading and reverse grading result from debris and hyper-concentrated turbidity flows (Sohn et al., 2001; Liu et al., 2015).

5.1.3 Deposition of Unit 3

The deposition of Unit 3 occurred in an alluvial fan-to-lake setting with gradually deepening water depths (Figure 6). Unit 3 consists of subunits 3a and 3b. Unit 3a is clast-dominated with a muddy matrix, and Unit 3b is a planar bedded mud layer.

In the CR01 core (Lim et al., 2021), the lake sediments were up to 72 m thick and contained well-developed planar laminae and bedding. The distance between the locations of the 20CR05 and 20HCR04 cores is 1.35 km, and these locations are at a similar altitude of 21.7 m (Figures 1C, D). The 20CR01 core records a stable lake environment, whereas the 20HCL04 core records sediment influx from surrounding slopes (Figure 1D). Thus, the 20CR01 core only contains fine-grained material transported by suspension in the lake waters. These fine-grained sediments were deposited in Unit 3 (Figure 7).

The uppermost part of Unit 3b contains tephra (i.e., glass shards), which is either airfall or reworked material. The absence of other reworked sediments in the tephra suggests that it is a primary airfall deposit. Only the upper part of the tephra layer (Mt facies) is found at other sites in the Hapcheon Basin. This tephra needs further research to determine its source and age.

5.1.4 Deposition of Unit 4

The deposition of Unit 4 was characterized by a gradual change from a deep lake setting to the present-day subaerial alluvial fan setting (Figure 6). Unit 4 consists of subunits 4a, 4b, and 4c. Unit 4a was deposited in a subaqueous environment that changed from a deep to a shallow lake. Unit 4b was deposited in a subaqueous to subaerial environment proximal to an alluvial fan or in a fluvial environment. Unit 4c was deposited in a subaerial alluvial fan and alluvial fan stream channels similar to the present-day setting.

The deposition of Unit 4 was associated with environmental changes caused by the sedimentary sources. Units 4a and 4b in a lake system were more affected by nearby slopes. The variability of the sedimentary sources can be attributed to different factors, such as climate change, relative erodibility of source rock types (Hooke and Rohrer, 1977), availability of surficial deposits within the drainage basin, and the rate and spatial distribution of subsidence (Allen and Hovius, 1998).

The sedimentary depositional environments of cores 20CR05 and 20HCL04 exhibit significant differences. Given that the altitudes of the two core locations are similar and that the lake depth remained the same, sediment infilling would occur first at the outer edge of the lake close to the crater rim. Eventually, the sedimentary accommodation space would have been filled in the interior of the crater (Figures 1D, 7). The coarsening-upward nature of the gravel units indicates increased flow competence and final fluvial deposition by powerful, boulder-transporting flood flows and subsequent debris flows. From the slopes or valley streams, the concentrated debris flow deposits covered the sheet deposits.

Unit 4c in core 20HCL04 represents deposition in a subaerial environment of an alluvial fan, and a correlated unit should be present in core CR05 as it would be difficult for deep water to exist at the 20CR05 core site at the same time.

Present-day geomorphological features were reported by Hwang and Yoon (2016) for the southern mountain slopes or valleys to the north of the three alluvial fan systems. Unit 4a (Figures 1C, D) is interpreted as having been deposited in an alluvial fan system that flowed down a valley from the northern slope. The alluvial fan means that the lake setting was no longer present or was only intermittent (Figure 7).

Therefore, by the time Unit 4 was deposited, the topography of the crater lake and basin had changed. The accommodation space created by the impact was infilled by the lower units. Subsequently, a watershed area similar to the present-day basin system became filled with alluvial fan deposits, such as the uppermost part of Unit 4a.

5.2 Quaternary geological implications of sediments in the Hapcheon impact crater

Sedimentary records can provide information on geomorphology, as inferred from sedimentary processes and depositional environments, because sedimentary processes are controlled by source materials and sediment transport regimes, including hydrological conditions. Another important factor is the size of the drainage basin (Crosta and Frattini, 2004). Alluvial fan and lacustrine depositional environments are represented in the sedimentary record of the Hapcheon impact crater (Figure 7).

The diversity of geological and geomorphological conditions within the study area allowed the study of a wide range of conditions under which processes on alluvial fans occurred. However, this complexity conceals the relationships and interactions between the factors that control the sedimentary processes. The geomorphology of alluvial fans and drainage basins can provide insights into the evolution of an alluvial fan and the hydrological processes responsible for fan building. Alluvial fan morphology is a consequence of different processes (Hooke and Rohrer, 1977; Blair and McPherson, 2008), while drainage basin morphology controls these different processes (Kostaschuk et al., 1986; Harvey et al., 1999; Blair and McPherson, 2008). The reason for this is that sediment discharge out of a catchment increases with increasing drainage area.

The morphology of an impact crater is bowl-shaped rather than V-shaped. This shape is formed because the sedimentary accommodation space created by the meteorite collision is simultaneously filled with collision-related sediments and crushed bedrock. The bowl-shaped accommodation space is bordered by a rimmed platform, a steep-sloped rimmed boundary, and sediment sources consisting of fallback ejecta, melting breccias, and brecciated basement rocks. These source materials are reworked and deposited by sedimentary processes such as gravity flow into the crater until the accommodation space is filled. Therefore, the geomorphology can be gleaned from the sedimentary processes as seen in the sedimentary record (Figure 7).

Craters formed by meteorite collisions are usually filled with impact-shocked material that is dispersed immediately after the collision. This means that the sedimentary layer in the crater may indicate a younger age than the actual collision period, as it refers to the period when sedimentation began after the meteorite impact. This may mean that the

collision occurred much earlier than the ages reported by Lim et al. (2021), despite the small point of age dating results. Based on our results, the Hapcheon crater contained a lake of 1.3–0.5 Ma. This is the first reported paleo-lake in Korea from this period, and it may provide a record of past Quaternary climate change on the Korean Peninsula.

The pressure, magnitude, and nature of the meteorite collision involved in the generation of the Hapcheon impact crater are unknown. However, the core sediments of 20HCL04 may contain materials that could determine the nature of the meteorite collision, which should be the subject of further research.

The presence of the tephra layer is also important because it can be used as a marker bed in the studied basin. Moreover, this tephra is the first reported on land in Korea, and volcanic activity has not been reported on the Korean Peninsula during this period (after 0.5 Ma). This tephra layer needs to be further investigated to identify its source and implications for volcanic hazards in Korea.

6 Conclusions

The Hapcheon Basin is the first meteorite impact crater reported on the Korean Peninsula. A sedimentary record for the Hapcheon impact crater was reconstructed from core 20HCL04. After the impact, a lake setting developed in the crater, thus controlling the sediment sources, transport, and deposition from the crater wall to the interior. A clast-supported gravel layer was mainly found in Unit 1, which was the lower section of the 66-meter borehole; this was interpreted as the initial lake environment where a sediment layer flowed in from the slopes after the meteor impact. Unit 2 was mainly found a matrix-supported gravel layer. Sedimentation occurred in the lake margin environment as the lake's water depth deepened, and an upward fining structure was observed. Unit 3 was a mud layer with lamination and SSDS, which was interpreted as sedimentation occurring in a lake environment with deep water depth. The section's SSDS was mainly formed by tectonic activity, such as earthquakes or landslides. It is believed that the Hapcheon Basin was also affected by such a tectonic event. The very thick laminated sediment layer may have been formed in a stable lake environment where the sedimentation rate was very low. As a result, it is thought to contain a record of climate changes during the Quaternary period. In Unit 4, there was a transition to an alluvial fan environment as the lake water depth gradually decreased and outlets formed due to accumulation. Furthermore, the sediment layer developed due to some small stream activity.

The lake system persisted from 1.3 to 0.5 Ma, and the lake sediments record climatic changes and, possibly, earthquake and volcanic events. This provides further impetus to obtain sediment cores from the Hapcheon impact crater lake and undertake further research on these sediments.

Data availability statement

The original contributions presented in the study are included in the article/Supplementary Material. Further inquiries can be directed to the corresponding author.

Author contributions

Conceptualization, SS, J-YL, and W-HN; methodology, SS, HY, YC, and JK; writing—revising and editing, SS and J-YL; data curation, HY, and YC; supervision, J-YL. All authors contributed to the article and approved the version submitted for publication.

Funding

This research was funded by a grant (No. 23-3111-3) from the Geological Survey in the Korean Peninsula, and the publication of the geological maps and the Basic Research Project of the KIGAM were funded by the National Research Foundation of Korea. And partly by "This research was supported by Basic Science Research Program through the National Research Foundation of Korea (NRF) funded by the Ministry of Education (No. 2019R1A6A1A03033167) and National Research Foundation Korea (RS-2023-00211265)".

Acknowledgments

We thank Dr. Joo-Yong Lee in KIGAM for giving us the opportunity to utilize the X-ray CT facility.

Conflict of interest

The authors declare that the research was conducted in the absence of any commercial or financial relationships that could be construed as a potential conflict of interest.

Publisher's note

Supplementary material

The Supplementary Material for this article can be found online at: https://www.frontiersin.org/articles/10.3389/feart.2023.1102785/full#supplementary-material

SUPPLEMENTARY FIGURE S1
Photographs of the 20HCL04 drill core samples from 0 to 66 m depth.

SUPPLEMENTARY FIGURE S2
X-ray computed tomography (CT) images of the 20HCL04 drill core samples.

References

Al-Sarawi, A. M. (1988). Morphology and facies of alluvial fans in kadhmah bay, Kuwait. *SEPM J. Sediment. Res.* 58, 902–907. doi:10.1306/212f8ea9-2b24-11d7-8648000102c1865d

Allen, P. A., and Hovius, N. (1998). Sediment supply from landslide-dominated catchments: Implications for basin-margin fans. *Basin Res.* 10, 19–35. doi:10.1046/j.1365-2117.1998.00060.x

Alván, A., and von Eynatten, H. (2014). Sedimentary facies and stratigraphic architecture in coarse-grained deltas: Anatomy of the Cenozoic Camaná Formation, southern Peru (16°25′S to 17°15′S). *J. S. Am. Earth Sci.* 54, 82–108. doi:10.1016/j.jsames.2014.04.008

Andrews, S. D., and Hartley, A. J. (2015). The response of lake margin sedimentary systems to climatically driven lake level fluctuations: Middle Devonian, Orcadian Basin, Scotland. *Sedimentology* 62, 1693–1716. doi:10.1111/sed.12200

Balco, G., and Shuster, D. L. (2009). 26Al–10Be–21Ne burial dating. *Earth Planet. Sci. Lett.* 286 (3–4), 570–575. doi:10.1016/j.epsl.2009.07.025

Barrett, B. J., Gawthorpe, R. L., Collier, R. E. L., Hodgson, D. M., and Cullen, T. M. (2020). Syn-rift delta interfan successions: Archives of sedimentation and basin evolution. *Depositional Rec.* 6, 117–143. doi:10.1002/dep2.95

Blair, T. C., and Mcpherson, J. G. (2008). Quaternary sedimentology of the Rose Creek fan delta, Walker Lake, Nevada, USA, and implications to fan-delta facies models. *Sedimentology* 55, 579–615. doi:10.1111/j.1365-3091.2007.00913.x

Bouma, A. H. (2000). Coarse-grained and fine-grained turbidite systems as end member models: Applicability and dangers. *Mar. Petrol Geol.* 17, 137–143. doi:10.1016/S0264-8172(99)00020-3

Chen, X. Y., Blockley, S. P. E., Fletcher, R., Zhang, S., Kim, J. H., Park, M. H., et al. (2022). Holocene tephrostratigraphy in the east sea/Japan sea: Implications for eruptive history of ulleungdo volcano and potential for hemispheric synchronization of sedimentary archives. *J. Geophys Res-Sol Ea.* 127, e2021JB023243. ARTN e2021JB023243. doi:10.1029/2021jb023243

Cheon, Y., Cho, H., Ha, S., Kang, H. C., Kim, J. S., and Son, M. (2019). Tectonically controlled multiple stages of deformation along the yangsan fault zone, SE Korea, since late cretaceous. *J. Asian Earth Sci.* 170, 188–207. doi:10.1016/j.jseaes.2018.11.003

Cheon, Y., Ha, S., Lee, S., and Son, M. (2020). Tectonic evolution of the cretaceous gyeongsang back-arc basin, SE Korea: Transition from sinistral transtension to strike-slip kinematics. *Gondwana Res.* 83, 16–35. doi:10.1016/j.gr.2020.01.012

Choi, S. H., Lee, J.-H., Kim, S.-S., Yu, J., and Puchtel, I. S. (2022b). Meteoritic component in impact breccias of the Jeokjung-Chogye structure, Republic of Korea: Evidence from the HSE abundances and ReOs isotopic systematics. *Chem. Geol.* 613, 121145. doi:10.1016/j.chemgeo.2022.121145

Choi, S., Kim, S.-W., Choi, E.-K., and Lee, Y.-C. (2022a). Estimating the impact process of the Jeokjung-Chogye Basin in Korea from gravity field interpretation. *Geophys J. Int.* 228, 1457–1463. doi:10.1093/gji/ggab410

Chough, S. K., and Sohn, Y. K. (2010). Tectonic and sedimentary evolution of a Cretaceous continental arc–backarc system in the Korean Peninsula: New view. *Earth-Sci Rev.* 101, 225–249. doi:10.1016/j.earscirev.2010.05.004

Chun, J. H., and Cheong, D. (2020). Origin of compositional diversity of marine tephra during the late middle pleistocene B-KY1 baekdusan volcanic eruption. *Appl. Sci-Basel* 10, 4469. ARTN 4469. doi:10.3390/app10134469

Crosta, G. B., and Frattini, P. (2004). Controls on modern alluvial fan processes in the central Alps, northern Italy. *Earth Surf. Proc. Land* 29, 267–293. doi:10.1002/esp.1009

Ebinghaus, A., Jolley, D. W., Andrews, S. D., and Kemp, D. B. (2017). Lake sedimentological and ecological response to hyperthermals: Boltysh impact crater, Ukraine. *Sedimentology* 64, 1465–1487. doi:10.1111/sed.12360

Fanetti, D., Anselmetti, F. S., Chapron, E., Sturm, M., and Vezzoli, L. (2008). Megaturbidite deposits in the holocene basin fill of lake como (southern alps, Italy). *Palaeogeogr. Palaeoclimatol. Palaeoecol.* 259, 323–340. doi:10.1016/j.palaeo.2007.10.014

Francke, A., Wagner, B., Just, J., Leicher, N., Gromig, R., Baumgarten, H., et al. (2016). Sedimentological processes and environmental variability at Lake Ohrid (Macedonia, Albania) between 637 ka and the present. *Biogeosciences* 13, 1179–1196. doi:10.5194/bg-13-1179-2016

Fredriksson, K., Dube, A., Milton, D. J., and Balasundaram, M. S. (1973). Lonar Lake, India: An impact Crater in basalt. *Science* 180, 862–864. doi:10.1126/science.180.4088.862

Fujioka, T., Chappell, J., Fifield, L. K., and Rhodes, E. J. (2009). Australian desert dune fields initiated with PlioceneePleistocene global climatic shift. *Geology* 37, 51–54. doi:10.1130/G25042A.1

Gao, C., Ji, Y., Wu, C., Jin, J., Ren, Y., Yang, Z., et al. (2019). Facies and depositional model of alluvial fan dominated by episodic flood events in arid conditions: An example from the Quaternary Poplar Fan, north-Western China. *Sedimentology* 67, 1750–1796. doi:10.1111/sed.12684

Gao, Y., Jiang, Z. X., Best, J. L., and Zhang, J. G. (2020). Soft-sediment deformation structures as indicators of tectono-volcanic activity during evolution of a lacustrine basin: A case study from the upper triassic ordos basin, China. *Mar. Petrol Geol.* 115. ARTN 104250. doi:10.1016/j.marpetgeo.2020.104250

Ghibaudo, G. (1992). Subaqueous sediment gravity flow deposits - practical criteria for their field description and classification. *Sedimentology* 39, 423–454. doi:10.1111/j.1365-3091.1992.tb02126.x

Granger, D. E. (2014). "Cosmogenic nuclide burial dating in archaeology and paleoanthropology," in *Treatise on geochemistry*. Editors H. D Holland and K. K Turekian. Second Edition (Oxford: Elsevier), 81e97.

Granger, D. E., Kirchner, J. W., and Finkel, R. C. (1997). Quaternary downcutting rate of the New River, Virginia, measured from differential decay of cosmogenic 26Al and 10Be in cave-deposited alluvium. *Geology* 25, 107. doi:10.1130/0091-7613(1997)025<0107:qdrotn>2.3.co;2

Granger, D. E., Lifton, N. A., and Willenbring, J. K. (2013). A cosmic trip: 25 years of cosmogenic nuclides in geology. *Geol. Soc. Am. Bull.* 125, 1379–1402. doi:10.1130/b30774.1

Granger, D. E., and Muzikar, P. F. (2001). Dating sediment burial with *in situ*-produced cosmogenic nuclides: Theory, techniques, and limitations. *Earth Planet. Sci. Lett.* 188, 269–281. doi:10.1016/s0012-821x(01)00309-0

Gurov, E. P., Koeberl, C., and Yamnichenko, A. (2007). El'gygytgyn impact crater, Russia: Structure, tectonics, and morphology. *Meteorit. Planet. Sci.* 42, 307–319. doi:10.1111/j.1945-5100.2007.tb00235.x

Guyard, H., St-Onge, G., Pienitz, R., Francus, P., Zolitschka, B., Clarke, G. K. C., et al. (2011). New insights into late pleistocene glacial and postglacial history of northernmost ungava (Canada) from pingualuit crater lake sediments. *Quat. Sci. Rev.* 30, 3892–3907. doi:10.1016/j.quascirev.2011.10.002

Hagemans, K., Nooren, K., de Haas, T., Córdova, M., Hennekam, R., Stekelenburg, M. C. A., et al. (2021). Patterns of alluvial deposition in Andean lake consistent with ENSO trigger. *Quat. Sci. Rev.* 259, 106900. doi:10.1016/j.quascirev.2021.106900

Harvey, A. M., Wigand, P. E., and Wells, S. G. (1999). Response of alluvial fan systems to the late pleistocene to holocene climatic transition: Contrasts between the margins of pluvial lakes lahontan and mojave, Nevada and California, USA. *Catena* 36, 255–281. doi:10.1016/S0341-8162(99)00049-1

Heller, P. L., and Paola, C. (1996). Downstream changes in alluvial architecture: An exploration of controls on channel-stacking patterns. *J. Sediment. Res.* 66, 297–306. doi:10.1306/D4268333-2B26-11D7-8648000102C1865D

Heward, A. P. (1978). Alluvial fan and lacustrine sediments from the Stephanian A and B (La Magdalena, Cinera-Matallana and Sabero) coalfields, northern Spain. *Sedimentology* 25, 451–488. doi:10.1111/j.1365-3091.1978.tb02076.x

Hong, W., Park, J. H., Kim, K. J., Woo, H. J., Kim, J. K., Choi, H. W., et al. (2010). Establishment of chemical preparation methods and development of an automated reduction system for ams sample preparation at kigam. *Radiocarbon* 52, 1277–1287. doi:10.1017/S0033822200046361

Hooke, R. L., and Rohrer, W. L. (1977). Relative erodibility of source-area rock types, as determined from second-order variations in alluvial-fan size. *Geol. Soc. Am. Bull.* 88, 1177–1182. doi:10.1130/0016-7606(1977)88<1177:Reosrt>2.0.Co;2

Horton, B. K., and Schmitt, J. G. (1996). Sedimentology of a lacustrine fan-delta system, miocene horse camp formation, Nevada, USA. *Sedimentology* 43, 133–155. doi:10.1111/j.1365-3091.1996.tb01464.x

Hwang, S., and Yoon, S. O. (2016). Geomorphic development of the jeogchung·chogye Basin and inner alluvial fan, Hapcheon, Republic of Korea. *J. Korean Assoc. regional Geogr.* 22, 225–239. (in Korean with English abstract).

Ikehara, K. (2015). Marine tephra in the Japan Sea sediments as a tool for paleoceanography and paleoclimatology. *Prog. Earth Planet. Sci.* 2, 36. ARTN 36. doi:10.1186/s40645-015-0068-z

Ineson, J. R. (1989). Coarse-grained submarine fan and slope apron deposits in a cretaceous back-arc basin, Antarctica. *Sedimentology* 36, 793–819. doi:10.1111/j.1365-3091.1989.tb01747.x

Jiang, H. C., Zhong, N., Li, Y. H., Xu, H. Y., Yang, H. L., and Peng, X. P. (2016). Soft sediment deformation structures in the Lixian lacustrine sediments, eastern Tibetan Plateau and implications for postglacial seismic activity. *Sediment. Geol.* 344, 123–134. doi:10.1016/j.sedgeo.2016.06.011

Jin, Z., Bickle, M. J., Chapman, H. J., Yu, J., Wang, S., and Chen, S. (2009). Early to mid-Pleistocene ostracod δ18O and δ13C in the central Tibetan Plateau: Implication for Indian monsoon change. *Palaeogeogr. Palaeoclimatol. Palaeoecol.* 280, 406–414. doi:10.1016/j.palaeo.2009.06.028

Jones, W. B., Bacon, M., and Hastings, D. A. (1981). The Lake Bosumtwi impact crater, Ghana. *Geol. Soc. Am. Bull.* 92, 342–349. doi:10.1130/0016-7606(1981)92<342:Tlbicg>2.0.Co;2

Juschus, O., Pavlov, M., Schwamborn, G., Preusser, F., Fedorov, G., and Melles, M. (2011). Late quaternary lake-level changes of lake el'gygytgyn, NE siberia. *Quat. Res.* 76, 441–451. doi:10.1016/j.yqres.2011.06.010

Kerr, S. J., Stanistreet, I. G., and Partridge, T. C. (1993). The sedimentary facies record from the Pretoria Saltpan crater. *South Afr. J. Sci.* 89, 372–374. doi:10.10520/AJA00382353_9263

Kim, J. C., Duller, G. A. T., Roberts, H. M., Wintle, A. G., Lee, Y. I., and Yi, S. B. (2010). Re-evaluation of the chronology of the palaeolithic site at Jeongokri, Korea, using OSL and TT-OSL signals from quartz. *Quat. Geochronol.* 5, 365–370. doi:10.1016/j.quageo.2009.02.005

Kim, J. C., Eum, C. H., Yi, S., Kim, J. Y., Hong, S. S., and Lee, J.-Y. (2012). Optically stimulated luminescence dating of coastal sediments from southwestern Korea. *Quat. Geochronol.* 10, 218–223. doi:10.1016/j.quageo.2012.03.008

Kim, J. W., and Chough, S. K. (2000). A gravel lobe deposit in the prodelta of the Doumsan fan delta (Miocene), SE Korea. *Sediment. Geol.* 130, 183–203. doi:10.1016/S0037-0738(99)00111-6

Kohl, C. P., and Nishiizumi, K. (1992). Chemical isolation of quartz for measurement of *in-situ* -produced cosmogenic nuclides. *Geochimica Cosmochimica Acta* 56, 3583–3587. doi:10.1016/0016-7037(92)90401-4

Komatsu, G., Kumar, P. S., Goto, K., Sekine, Y., Giri, C., and Matsui, T. (2014). Drainage systems of Lonar Crater, India: Contributions to Lonar Lake hydrology and crater degradation. *Planet. Space Sci.* 95, 45–55. doi:10.1016/j.pss.2013.05.011

Kostaschuk, R. A., Macdonald, G. M., and Putnam, P. E. (1986). Depositional process and alluvial fan-drainage basin morphometric relationships near banff, alberta, Canada. *Earth Surf. Proc. Land* 11, 471–484. doi:10.1002/esp.3290110502

Lee, C., Kim, J. C., Park, J. H., Kim, I. C., Kang, J., Cheoun, M. K., et al. (2000). Progress in sample preparation system for the Seoul National University AMS facility. *Nucl. Instrum. Methods Phys. Res. Sect. B Beam Interact. Mater. Atoms* 172, 454–457. doi:10.1016/S0168-583X(00)00395-5

Li, C. L., Chen, P. P., Liu, J. M., Fu, H. T., Zhang, J. L., and Xie, J. (2016). The coarse-grained lacustrine slope apron deposits in the moliqing area, yitong basin, northeast China. *Acta Geol. Sin-Engl* 90, 1809–1820. doi:10.1111/1755-6724.12818

Lim, J., Hong, S. S., Han, M., Yi, S., and Kim, S. W. (2021). First finding of impact cratering in the Korean Peninsula. *Gondwana Res.* 91, 121–128. doi:10.1016/j.gr.2020.12.004

Liu, B., Tan, C., Yu, X., Qu, J., Zhao, X., and Zhang, L. (2019). Sedimentary characteristics and controls of a retreating, coarse-grained fan-delta system in the Lower Triassic, Mahu Depression, northwestern China. *Geol. J.* 54, 1141–1159. doi:10.1002/gj.3215

Liu, F., Zhu, X. M., Li, Y., Xu, L. M., Niu, X. B., Zhu, S. F., et al. (2015). Sedimentary characteristics and facies model of gravity flow deposits of Late Triassic Yanchang Formation in southwestern Ordos Basin, NW China. *Petroleum Explor. Dev.* 42, 633–645. doi:10.1016/S1876-3804(15)30058-6

Liu, K. X., Chen, M., Ding, X. F., Fu, D. P., Ding, P., Shen, C. D., et al. (2013). AMS radiocarbon dating of lacustrine sediment from an impact crater in northeastern China. *Nucl. Instrum. Methods Phys. Res. Sect. B Beam Interact. Mater. Atoms* 294, 593–596. doi:10.1016/j.nimb.2012.08.043

Losiak, A., Wild, E. M., Geppert, W. D., Huber, M. S., Jõeleht, A., Kriiska, A., et al. (2016). Dating a small impact crater: An age of Kaali crater (Estonia) based on charcoal emplaced within proximal ejecta. *Meteorit. Planet. Sci.* 51, 681–695. doi:10.1111/maps.12616

Machida, H. (1999). The stratigraphy, chronology and distribution of distal marker-tephras in and around Japan. *Glob. Planet Change* 21, 71–94. doi:10.1016/S0921-8181(99)00008-9

Mader, M. M., and Osinski, G. R. (2018). Impactites of the Mistastin Lake impact structure: Insights into impact ejecta emplacement. *Meteorit. Planet. Sci.* 53, 2492–2518. doi:10.1111/maps.13173

Maharjan, S., Shrestha, P., and Tamrakar, N. K. (1970). Facies association and depositional environment of fan-delta sequence in southwest Kathmandu Basin, Nepal. *Bull. Dep. Geol.* 12, 1–16. doi:10.3126/bdg.v12i0.2246

Marcolla, A., Miola, A., Mozzi, P., Monegato, G., Asioli, A., Pini, R., et al. (2021). Middle Pleistocene to Holocene palaeoenvironmental evolution of the south-eastern Alpine foreland basin from multi-proxy analysis. *Quat. Sci. Rev.* 259, 106908. doi:10.1016/j.quascirev.2021.106908

Masaitis, V. L. (2005). Morphological, structural and lithological records of terrestrial impacts: An overview. *Aust. J. Earth Sci.* 52, 509–528. doi:10.1080/08120090500170427

Matsu'ura, T., Kimura, J. I., Chang, Q., and Komatsubara, J. (2017). Using tephrostratigraphy and cryptotephrostratigraphy to re-evaluate and improve the Middle Pleistocene age model for marine sequences in northeast Japan (Chikyu C9001C). *Quat. Geochronol.* 40, 129–145. doi:10.1016/j.quageo.2016.11.001

McLean, D., Albert, P. G., Nakagawa, T., Suzuki, T., Staff, R. A., Yamada, K., et al. (2018). Integrating the Holocene tephrostratigraphy for East Asia using a high-resolution cryptotephra study from Lake Suigetsu (SG14 core), central Japan. *Quat. Sci. Rev.* 183, 36–58. doi:10.1016/j.quascirev.2017.12.013

McLean, D., Albert, P. G., Suzuki, T., Nakagawa, T., Kimura, J. I., Chang, Q., et al. (2020). Refining the eruptive history of Ulleungdo and Changbaishan volcanoes (East Asia) over the last 86 kyrs using distal sedimentary records. *J. Volcanol. Geoth Res.* 389, 106669. ARTN 106669. doi:10.1016/j.jvolgeores.2019.106669

Melles, M., Brigham-Grette, J., Minyuk, P., Koeberl, C., Andreev, A., Cook, T., et al. (2011). The Lake el'gygytgyn scientific drilling Project – conquering arctic challenges through continental drilling. *Sci. Dril* 11, 29–40. doi:10.2204/iodp.sd.11.03.2011

Miall, A. D. (2006). *The geology of fluvial deposits: Sedimentary facies, basin analysis, and petroleum geology*. Berlin: Springer.

Moscariello, A., Ravazzi, C., Brauer, A., Mangili, C., Chiesa, S., Rossi, S., et al. (2000). A long lacustrine record from the piànico-sèllere basin (Middle-Late pleistocene, northern Italy). *Quatern Int.* 73-74, 47–68. doi:10.1016/S1040-6182(00)00064-1

Mulder, T., and Alexander, J. (2001). The physical character of subaqueous sedimentary density flows and their deposits. *Sedimentology* 48, 269–299. doi:10.1046/j.1365-3091.2001.00360.x

Nelson, C. H., Meyer, A. W., Thor, D., and Larsen, M. (1986). crater lake, Oregon: A restricted basin with base-of-slope aprons of nonchannelized turbidites. *Geology* 14, 238–241. doi:10.1130/0091-7613(1986)14<238:cloarb>2.0.co;2

Nemec, W., and Postma, G. (1993). "Quaternary alluvial fans in southwestern crete: Sedimentation processes and geomorphic evolution," in *Alluvial sedimentation. International association of sedimentologists* (Hoboken: John Wiley & Sons), 235–276.

Nishiizumi, K., Imamura, M., Caffee, M. W., Southon, J. R., Finkel, R. C., and McAninch, J. (2007). Absolute calibration of 10Be AMS standards. *Nucl. Instrum. Methods Phys. Res. Sect. B Beam Interact. Mater. Atoms* 258, 403–413. doi:10.1016/j.nimb.2007.01.297

Nishiizumi, K. (2004). Preparation of 26Al AMS standards. *Nucl. Instrum. Methods Phys. Res. Sect. B Beam Interact. Mater. Atoms* 223-224, 388–392. doi:10.1016/j.nimb.2004.04.075

Osinski, G. R., Bunch, T. E., Flemming, R. L., Buitenhuis, E., and Wittke, J. H. (2015). Impact melt- and projectile-bearing ejecta at Barringer Crater, Arizona. *Earth Planet S. C. Lett.* 432, 283–292. doi:10.1016/j.epsl.2015.10.021

Osinski, G. R., Cockell, C. S., Pontefract, A., and Sapers, H. M. (2020). The role of meteorite impacts in the origin of life. *Astrobiology* 20, 1121–1149. doi:10.1089/ast.2019.2203

Osinski, G. R., Grieve, R. A. F., Bleacher, J. E., Neish, C. D., Pilles, E. A., and Tornabene, L. L. (2018). Igneous rocks formed by hypervelocity impact. *J. Volcanol. Geoth Res.* 353, 25–54. doi:10.1016/j.jvolgeores.2018.01.015

Osinski, G. R., Grieve, R. A. F., Ferriere, L., Losiak, A., Pickersgill, A. E., Cavosie, A. J., et al. (2022). Impact Earth: A review of the terrestrial impact record. *Earth-Sci Rev.* 232, 104112. ARTN 104112. doi:10.1016/j.earscirev.2022.104112

Osinski, G. R. (2004). Impact melt rocks from the ries structure, Germany: An origin as impact melt flows? *Earth Planet S. C. Lett.* 226, 529–543. doi:10.1016/j.epsl.2004.08.012

Osinski, G. R., and Lee, P. (2005). Intra-crater sedimentary deposits at the haughton impact structure, devon island, Canadian high arctic. *Meteorit. Planet. Sci.* 40, 1887–1899. doi:10.1111/j.1945-5100.2005.tb00152.x

Parnell, J., Taylor, C. W., Thackrey, S., Osinski, G. R., and Lee, P. (2010). Permeability data for impact breccias imply focussed hydrothermal fluid flow. *J. Geochem. Explor.* 106, 171–175. doi:10.1016/j.gexplo.2009.12.002

Pope, R., Wilkinson, K., Skourtsos, E., Triantaphyllou, M., and Ferrier, G. (2008). Clarifying stages of alluvial fan evolution along the Sfakian piedmont, southern Crete: New evidence from analysis of post-incisive soils and OSL dating. *Geomorphology* 94, 206–225. doi:10.1016/j.geomorph.2007.05.007

Rana, N., Sati, S. P., Sundriyal, Y., and Juyal, N. (2016). Genesis and implication of soft-sediment deformation structures in high-energy fluvial deposits of the Alaknanda Valley, Garhwal Himalaya, India. *Sediment. Geol.* 344, 263–276. doi:10.1016/j.sedgeo.2016.06.012

Reimer, P. J., Bard, E., Bayliss, A., Beck, J. W., Blackwell, P. G., Ramsey, C. B., et al. (2013). IntCal13 and Marine13 radiocarbon age calibration curves 0–50,000 Years cal BP. *Radiocarbon* 55, 1869–1887. doi:10.2458/azu_js_rc.55.16947

Reimold, W. U., and Koeberl, C. (2014). Impact structures in africa: A review. *J. Afr. Earth Sci.* 93, 57–175. doi:10.1016/j.jafrearsci.2014.01.008

Reimold, W. U., Koeberl, C., and Reddering, J. S. V. (1998). The 1992 drill core from the kalkkop impact crater, eastern cape province, South Africa: Stratigraphy, petrography, geochemistry and age. *J. Afr. Earth Sci.* 26, 573–592. doi:10.1016/S0899-5362(98)00034-7

Retzler, A. J., Tapanila, L., Steenberg, J. R., Johnson, C. J., and Myers, R. A. (2015). Post-impact depositional environments as a proxy for crater morphology, Late Devonian Alamo impact, Nevada. *Geosphere* 11, 123–143. doi:10.1130/ges00964.1

Ridgway, K. D., and Decelles, P. G. (1993). Stream-dominated alluvial-fan and lacustrine depositional systems in cenozoic strike-slip basins, denali fault system, yukon-territory, Canada. *Sedimentology* 40, 645–666. doi:10.1111/j.1365-3091.1993.tb01354.x

Ritter, J. B., Miller, J. R., and Husek-Wulforst, J. (2000). Environmental controls on the evolution of alluvial fans in Buena Vista Valley, North Central Nevada, during late quaternary time. *Geomorphology* 36, 63–87. doi:10.1016/S0169-555x(00)00048-9

Roberts, H. M. (2007). Assessing the effectiveness of the double-SAR protocol in isolating a luminescence signal dominated by quartz. *Radiat. Meas.* 42, 1627–1636. doi:10.1016/j.radmeas.2007.09.010

Shaar, R., Matmon, A., Horwitz, L. K., Ebert, Y., Chazan, M., Arnold, M., et al. (2021). Magnetostratigraphy and cosmogenic dating of Wonderwerk cave: New constraints for

the chronology of the South African earlier stone age. *Quat. Sci. Rev.* 259, 106907. doi:10.1016/j.quascirev.2021.106907

Shanahan, T. M., Beck, J. W., Overpeck, J. T., McKay, N. P., Pigati, J. S., Peck, J. A., et al. (2012). Late Quaternary sedimentological and climate changes at Lake Bosumtwi Ghana: New constraints from laminae analysis and radiocarbon age modeling. *Palaeogeogr. Palaeoclimatol. Palaeoecol.* 361-362, 49–60. doi:10.1016/j.palaeo.2012.08.001

Shultz, A. W. (1984). Subaerial debris-flow deposition in the upper paleozoic cutler formation, Western Colorado. *J. Sediment. Res.* 54, 759–772. doi:10.1306/212f84ef-2b24-11d7-8648000102c1865d

Sletten, K., Blikra, L. H., Ballantyne, C. K., Nesje, A., and Dahl, S. O. (2003). Holocene debris flows recognized in a lacustrine sedimentary succession: Sedimentology, chronostratigraphy and cause of triggering. *Holocene* 13, 907–920. doi:10.1191/0959683603hl673rp

Sohn, Y. K., Rhee, C. W., and Shon, H. (2001). Revised stratigraphy and reinterpretation of the miocene pohang basinfill, SE Korea: Sequence development in response to tectonism and eustasy in a back-arc basin margin. *Sediment. Geol.* 143, 265–285. doi:10.1016/S0037-0738(01)00100-2

Stone, J. O. (2000). Air pressure and cosmogenic isotope production. *J. Geophys. Res.* 105, 23753–23759. doi:10.1029/2000jb900181

Talling, P. J., Masson, D. G., Sumner, E. J., and Malgesini, G. (2012). Subaqueous sediment density flows: Depositional processes and deposit types. *Sedimentology* 59, 1937–2003. doi:10.1111/j.1365-3091.2012.01353.x

Tha, H., Wysocka, A., Pha, P., Cuong, N., and Ziółkowski, P. (2015). Lithofacies and depositional environments of the paleogene/neogene sediments in the hoanh bo basin (quang ninh province, NE vietnam). *Geol. Geophys. Environ.* 41, 353. doi:10.7494/geol.2015.41.4.353

Tinterri, R., Magalhaes, P. M., Tagliaferri, A., and Cunha, R. S. (2016). Convolute laminations and load structures in turbidites as indicators of flow reflections and decelerations against bounding slopes. Examples from the Marnoso-arenacea Formation (northern Italy) and Annot Sandstones (south eastern France). *Sediment. Geol.* 344, 382–407. doi:10.1016/j.sedgeo.2016.01.023

Tu, H., Shen, G., Li, H., Xie, F., and Granger, D. E. (2015). 26Al/10Be burial dating of Xujiayao Houjiayao site in Nihewan basin, northern Chine. *PLoS One* 10, e0118315. Lebatard et al., 2019. doi:10.1371/journal.pone.0118315

Wang, K., Xu, X., Sun, X., Tu, H., Zeng, Q., Lu, Y., et al. (2019). Cosmogenic nuclide burial dating of Liuwan Paleolithic site in the Luonan basin, Central China. *J. Geogr. Sci.* 29, 406–416. doi:10.1007/s11442-019-1606-1

Wennrich, V., Minyuk, P. S., Borkhodoev, V., Francke, A., Ritter, B., Nowaczyk, N. R., et al. (2014). Pliocene to Pleistocene climate and environmental history of Lake El'gygytgyn, Far East Russian Arctic, based on high-resolution inorganic geochemistry data. *Clim. Past.* 10, 1381–1399. doi:10.5194/cp-10-1381-2014

Winsemann, J., Hartmann, T., Lang, J., Fälber, R., and Lauer, T. (2022). Depositional architecture and aggradation rates of sand-rich, supercritical alluvial fans: Control by autogenic processes or high-frequency climatic oscillations? *Sediment. Geol.* 440, 106238. doi:10.1016/j.sedgeo.2022.106238

Wintle, A. G., and Murray, A. S. (2006). A review of quartz optically stimulated luminescence characteristics and their relevance in single-aliquot regeneration dating protocols. *Radiat. Meas.* 41, 369–391. doi:10.1016/j.radmeas.2005.11.001

Ye, M. S., Xie, X. N., Swennen, R., Xu, C. G., Du, X. F., and Du, X. B. (2021). Depositional characteristics of a lacustrine mixed sediment system: A case study from the eastern shijiutuo uplift, offshore bohai bay basin, eastern China. *J. Asian Earth Sci.* 209, 104671. ARTN 104671. doi:10.1016/j.jseaes.2021.104671

Yu, S. Y., Du, J. H., Hou, Z. F., and Colman, S. M. (2019). Late-Quaternary dynamics and palaeoclimatic implications of an alluvial fan-lake system on the southern Alxa Plateau, NW China. *Geomorphology* 327, 1–13. doi:10.1016/j.geomorph.2018.10.012

Zolitschka, B., Francus, P., Ojala, A. E. K., and Schimmelmann, A. (2015). Varves in lake sediments—a review. *Quat. Sci. Rev.* 117, 1–41. doi:10.1016/j.quascirev.2015.03.019